Emergent Materials (2025) 8:5765–5775
https://doi.org/10.1007/s42247-025-01277-4

ORIGINAL ARTICLE

Tailored plasmonic gold nanoparticles coated with manganese oxide for selective light-driven oxidation of 5-hydroxymethylfurfural

Arthur Reymond[1,2] · IbrahiM Abdelsalam[2] · Filippo Pieretti[3] · Nikolaos Dimitratos[3] · Almudena Marti[1] · Pedro H. C. Camargo[2] · Robert Wojcieszak[1]

Received: 21 May 2025 / Accepted: 30 September 2025 / Published online: 14 October 2025

Abstract

The development of efficient and selective nanocatalysts for biomass valorization is critical for advancing sustainable chemistry. Here, we report the colloidal synthesis of spherical gold nanoparticles (AuNPs) coated with manganese oxide (MnO_2) shells of tunable thicknesses (3.5, 5.0, 7.5, and 10.0 nm), forming Au@MnO_2 core-shell nanostructures with well-preserved plasmonic properties. Structural and spectroscopic characterization confirmed the successful fabrication and a red-shifted localized surface plasmon resonance (LSPR), indicative of MnO_2 shell formation. Supported on ZrO_2, the Au@MnO_2 catalysts exhibited enhanced activity and selectivity in the photocatalytic oxidation of 5-hydroxymethylfurfural (HMF) under 365 nm and 450 nm light, outperforming thermal conditions. The MnO_2 shell thickness and irradiation wavelength significantly influenced product distribution, favoring valuable oxidation intermediates. In addition to improved catalytic performance, the core-shell design provided enhanced stability. These findings highlight the potential of plasmonic core-shell nanostructures for light-driven biomass conversion and broader nanocatalysis applications.

Keywords Gold nanoparticles · Core-shell · Plasmonics · Photocatalysis · 5-hydroxymethylfurfural

1 Introduction

The development of efficient nanocatalysts for biomass valorization is critical for advancing chemistry. Nanocatalysis, leveraging the unique properties of metallic nanoparticles, offers high surface-to-volume ratios, tunable electronic structures, and light-harvesting capabilities [1–3]. Within this domain, plasmonic nanoparticles have enabled new paradigms in catalysis by converting visible light into localized energy via localized surface plasmon resonance (LSPR). This phenomenon, arising from the collective oscillation of conduction electrons under light irradiation, leads to strong, wavelength-selective absorption and the generation of energetic carriers or thermal effects that can promote chemical reactions under mild conditions [4–8]. Gold nanoparticles (AuNPs) are among the most studied plasmonic systems due to their chemical stability and LSPR in the visible region. Beyond control of size and shape, further functionalization through core-shell engineering allows integration of plasmonic and catalytic domains within a single nanostructure. In particular, coating AuNPs with manganese oxide (MnO_2, a low-cost, earth-abundant, and catalytically active semiconductor as shown in Fig. 1(a)) offers an attractive platform

✉ Arthur Reymond
arthur.reymond@univ-lorraine.fr

IbrahiM Abdelsalam
ibrahim.abdelsalam@helsinki.fi

Filippo Pieretti
filippo.pieretti@studenti.unicam.it

Nikolaos Dimitratos
nikolaos.dimitratos@unibo.it

Almudena Marti
almudena.marti-morant@univ-lorraine.fr

Pedro H. C. Camargo
pedro.camargo@helsinki.fi

Robert Wojcieszak
robert.wojcieszak@cnrs.fr

1 L2CM UMR 7053, Université de Lorraine, CNRS, Faculté des Sciences et Technologies, Vandœuvre-lès-Nancy 54506, France

2 Department of Chemistry, University of Helsinki, A. I. Virtasen aukio 1, PO Box 55, FIN-0014, Helsinki, Finland

3 Dipartimento di Chimica Industriale "Toso Montanari", Alma Mater Studiorum Università di Bologna, Viale Risorgimento 4, Bologna 40126, Italy

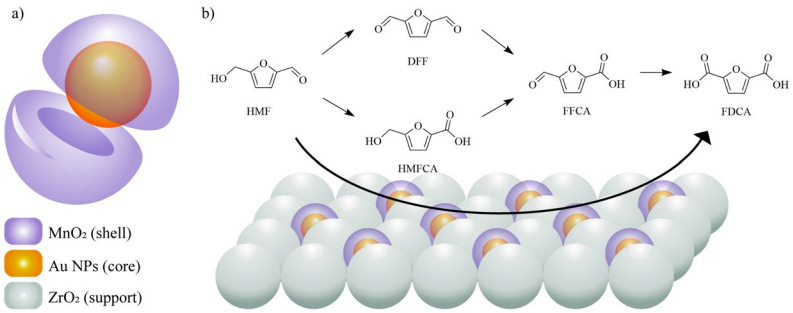

Fig. 1 (a) Schematic representation of the deposition of a shell layer onto the core of plasmonic nanoparticles. (b) Oxidation pathways in 5-hydroxymethylfurfural (HMF) oxidation on heterogeneous catalysts

for light-driven oxidation chemistry. The MnO_2 shell can be tuned in thickness to modulate the electronic and catalytic interactions with the Au core, while simultaneously enhancing structural stability and reaction selectivity [9–11].

Among biomass-derived platform molecules, 5-hydroxymethylfurfural (HMF) is a key molecule produced from cellulose. Its significance lies in its ability to serve as a precursor for the synthesis of a wide range of high-value-added chemicals, such as 2,5-furandicarboxylic acid (FDCA), 2,5-diformylfuran (DFF), 5-formyl-2-furancarboxylic acid (FFCA), and 5-hydroxymethyl-2-furancarboxylic acid (HMFCA) [12]. The reaction scheme presented in Fig. 1(b) illustrates the possible catalytic oxidation pathways occurring during the HMF oxidation to FDCA [13, 14]. This compound is of particular interest due to its applications in the production of bioplastics, notably polyethylene 2,5furandicarboxylate (PEF), which is a sustainable alternative to petroleum-derived polyethylene terephthalate (PET). FDCA has been recognized for its potential to replace petrochemical products in numerous industrial applications, highlighting the importance of HMF in efforts to reduce dependence on fossil resources and promote greener chemistry. Most previous studies have employed catalysts that require complex and costly synthesis, exhibit limited light utilization (primarily UV or thermal activation), and operate under high temperatures and pressures to achieve moderate product selectivity [15]. In contrast, this work aims to develop plasmonic hybrid core–shell catalysts with a simple and low-cost synthesis approach, enabling visible-light activation via the LSPR effect, and faciliting selective oxidation under ambient temperature and pressure [16]. While Au@MnO_2 core-shell nanoparticles have been reported, [17, 18] studies exploring the interplay between MnO_2 shell thickness, plasmonic effects, and HMF oxidation activity under controlled light wavelengths remain scarce. Furthermore, the impact of catalyst supports — such as ZrO_2, known for enhancing dispersion and reusability [19, 20] — has not been thoroughly investigated in this context.

In this work, we report the colloidal synthesis of spherical Au@MnO_2 nanocatalysts with systematically varied MnO_2 shell thicknesses (3.5-10 nm), followed by their integration onto ZrO_2 supports. Structural and optical characterizations confirmed the formation of well-defined core-shell architectures with preserved plasmonic features. The catalysts were evaluated for the selective photocatalytic oxidation of HMF under UV (365 nm) and visible (450 nm) irradiation, and benchmarked against thermal conditions. Our findings establish key structure-property-activity relationships and underline the potential of plasmon-assisted core-shell nanocatalysts for efficient, light-driven biomass valorization.

2 Experimental

2.1 Chemicals

All chemicals used in this study were of analytical grade and were used as received without further purification. Chloroauric acid trihydrate ($HAuCl_4 \cdot 3H_2O$, 99.9%, Sigma-Aldrich), sodium citrate tribasic dihydrate ($C_6H_5Na_3O_7 \cdot 3H_2O$, 99%, Sigma-Aldrich), potassium hydroxide (KOH, 85%, Sigma-Aldrich), sodium oxalate ($Na_2C_2O_4$, 99.5%, Fisher Scientific), potassium permanganate ($KMnO_4$, 99%, Sigma-Aldrich), zirconium(IV) oxide (ZrO_2 nanopowder, < 100 nm particle size, Sigma-Aldrich) and sodium hydroxide pellets (NaOH, 97% trace metal basis, Fisher Scientific UK) were used as received for the synthesis of nanoparticles and for various catalytic tests. Substrates and standards for catalytic evaluations included 5-hydroxymethylfurfural (HMF, $C_6H_6O_3$, $\geq$ 99%, Sigma-Aldrich), 2,5-furandicarboxylic acid (FDCA, $C_6H_4O_5$, 97%, Sigma-Aldrich), 5-hydroxymethyl-2-furancarboxylic acid (HMFCA, $C_6H_6O_4$, 97%, Sigma-Aldrich), 5-formyl-2-furancarboxylic acid (FFCA, $C_6H_6O_4$, 98%, Sigma-Aldrich), 2,5-furandicarboxaldehyde (DFF, $C_6H_4O_3$, 97%, Sigma-Aldrich). Deionized water (18.2 MΩ·cm) was used throughout the experiments, and all glassware was cleaned with aqua regia, using a 3:1 ratio of 15 mL HCl and 5 mL HNO_3.

2.2 Preparation of Spherical AuNPs

First, a 0.025 M gold precursor solution was prepared using $HAuCl_4$. To achieve this, 49.225 mg of gold precursor was weighed and dissolved in 5 mL of ultrapure water.

This solution dissolves almost instantly and remains stable over time, making it suitable for use in multiple future experiments.

Gold seeds were prepared using the citrate reduction method. In a typical procedure, 1 mL of the 0.025 M $HAuCl_4$ stock solution was added to a 100 mL volumetric flask and filled with pure water. This mixture was heated in a round-bottom flask under magnetic stirring at 800 rpm until it reached 110°C for 15 minutes [21]. Following this, 3 mL of a 1 wt.% sodium citrate dihydrate solution was added. In this case, sodium citrate acts as both a reducing agent and stabilizer. The reaction was allowed to proceed for an additional 20 minutes [22].

2.3 Core-shell of spherical AuNPs coated with MnO_2

The procedure was adapted from Oliveira et al. [23]. Initially, the required amount of $KMnO_4$ was calculated to achieve the desired MnO_2 layer thickness. The specific amounts of $KMnO_4$ for each target thickness are detailed in Table S1. The reduction of manganese (VII) was achieved using $Na_2C_2O_4$, with the concentration of oxalate maintained at one-fifth of the permanganate concentration. For the preparation of stock solutions, 7.9 mg of $KMnO_4$ and 6.7 mg of $Na_2C_2O_4$ were dissolved separately in 5 mL of water to make 10 mM solutions, and 14.03 mg of KOH was dissolved in 25 mL of water to make a 10 mM solution. Alternatively, 14.7 mg of $C_6H_5Na_3O_7{\cdot}3H_2O$ can be used instead of $Na_2C_2O_4$ in 5 mL of water to prepare a 10 mM solution, yielding similar results in terms of nanostructure formation.

In a 25 mL flask, placed in an ice bath and under magnetic stirring at 800 rpm, 10 mL of our spherical AuNPs solution were adjusted to a pH of 9.5-10.0 using the 10.0 mM KOH solution. In this instance, 3.5 mL of KOH was added. A specific volume of the 10.0 mM $KMnO_4$ solution and the 10.0 mM $Na_2C_2O_4$ solution were aliquoted according to the desired nominal thickness of MnO_2 and added sequentially to the AuNPs solution. Preparations for each of the described thicknesses were carried out.

The suspension was stirred at 800 rpm for 10 minutes in the ice bath, then transferred to a thermostatic bath set at 60.0°C for 2 hours. During this period, the color of the suspension changed from bright red to light purple, with the extent of the color change depending on the amount of $KMnO_4$ added. The synthesized nanoparticles were subsequently washed by centrifugation. Initially, the solution was distributed into 1 mL Eppendorf tubes and centrifuged for 20 minutes at 14,500 rpm. The supernatant was removed, and the nanoparticles were redispersed in water in the same Eppendorf tubes for another round of centrifugation for 10 minutes at 14,500 rpm. This process was repeated a second time. All the nanoparticles were then collected and dispersed in 2 mL of water for each of the preparations.

2.4 Synthesis of the supported Au@MnO_2/ZrO_2 catalysts

Once the Au@MnO_2 core-shell materials were synthesized, they were supported on ZrO_2. To achieve this, the same mass of Au@MnO_2 nanoparticles was supported for all four preparations. An equivalent mass of 1% of the ZrO_2 mass, which was set at 50 mg, was used. This mass of 50 mg and the mass percentage of 1% were chosen to ensure that a maximum volume of 2 mL, the volume of our dispersed preparations, could be used. Naturally, the mass of Au@MnO_2 corresponds to the sum of the masses of Au and MnO_2. Table S2 shows the volume of liquid to be taken to achieve this mass percentage.

To support the dispersed preparations, 50 mg of ZrO_2 were placed in a petri dish. Subsequently, 100 μL of the nanoparticle suspension was added, followed by gentle scratching to ensure even distribution. The petri dish was then placed in an oven at 60°C for 10 minutes. This process was repeated as many times as necessary to reach the required total volume of the suspension. Finally, the samples were left in the oven overnight at 60°C to thoroughly dry the powder.

2.5 Control experiments

Control experiments were conducted to validate the synthesis protocol using characterization tools. Specifically, the same procedure described above was performed twice with variations: in one case, the reaction was performed without potassium permanganate to evaluate its effect on the spherical gold nanoparticles; in the other case, the reaction was conducted without the gold precursor solution to observe the behavior of potassium permanganate in the absence of the Au core, thereby isolating the influence of the core–shell system.

2.6 Characterization of Au@MnO_2

The LSPR band of Au@MnO_2 nanoparticles was measured by absorption spectroscopy using the PerkinElmer Lambda 900 UV-Vis-NIR spectrometer. The samples were diluted in ultrapure water and measured against water as the reference. Scanning Electron Microscopy (SEM) was used to determine the surface topography and morphology of the prepared structures. SEM measurements were performed using a Hitachi S-4800 field emission scanning electron microscope, with an acceleration voltage of 10 kV and a working distance of 8 mm. All samples were prepared by adhering

them to an aluminum holder using conductive carbon tape. Transmission Electron Microscopy (TEM) was employed to determine the size and shape of the AuNP and Au@MnO_2. TEM was performed using the Hitachi S-4800 field emission transmission electron microscope with an acceleration voltage of 25 kV and a working distance of 8 mm. For sample preparation, a single drop was deposited onto a copper grid coated with a lacy carbon film. The powder X-ray diffraction (PXRD) data of the prepared NPs were collected using a Bruker D8 Advance in Bragg-Brentano geometry with Cu Kα radiation ($\lambda = 1.5406$ Å) and a Ni filter. Diffraction data were collected over a range of 20–70°, 2θ (with a step width of 0.02°, 2θ and a count time of 1 second per step). The diffraction patterns were indexed by comparison with the Joint Committee on Powder Diffraction Standards (JCPDS) files, allowing for the identification of the crystalline phases present in the samples.

2.7 Catalytic and photocatalytic tests

5 mg of catalyst were weighed on an analytical balance and then placed in a test tube. A solution of 25 mM HMF was prepared by weighing 78.75 mg of HMF in a 25 mL volumetric flask. Three molar equivalents of NaOH were added relative to the amount of HMF. The flask was brought to volume with ultrapure water and the pH was measured with pH paper and found to be 13. Then, 3 mL of this solution was withdrawn with a micropipette and added to each test tube containing the catalyst. Each of them was placed in the reactor with a magnetic stir bar to ensure stirring. The light was turned on at T_0. Two Asynt LightSyn Illumin 8 reactors were used: the first one operates at a wavelength of 365 nm and the second one operates at a wavelength of 450 nm. The lamps are composed of 8 LED COB light sources of 10 W each, operating at different wavelengths. Reactions were carried out for 4 hours at atmospheric pressure. During the tests under light illumination, the temperature of the solution was between 38 and 40°C. Each experiment was performed with mixing at a speed of 600 rpm. In the thermal catalysis experiment, the light was turned off and the temperature was set to 40°C. All other conditions were the same as above. After 4 hours, the reactors were switched off, and the test tubes and magnetic stir bars were removed. The solution containing the catalyst was filtered using a PTFE filter. To avoid problems related to exceeding the limit of quantification (LOQ) of the HPLC, the final solutions were diluted. For those experiments carried out without using NaOH, a dilution of 1:10 was made by taking 0.10 mL of the final solution and 0.90 mL of ultrapure water with a micropipette. Each aliquot was placed in a vial. Samples were analyzed by high-performance liquid chromatography (HPLC) using a ThermoScientific Vanquish with a UV detector at 265 nm. A BioRad Aminex HPX-87H-Organic Acids column was used at 40°C in isocratic elution mode (0.6 mL/min) with a 5 mM/L H_2SO_4 solution as the mobile phase. Each sample was analyzed using HPLC. The concentration of each reactant, intermediate, and product was determined according to the calibration curve using commercial samples as standards. The equations used for the calculation of the HMF conversion, product selectivity, and carbon balance (C.B.) were as follows:

$$\mathrm{HMF}_{\mathrm{conversion}} = \left(\frac{C_{\mathrm{HMF}_f} - C_{\mathrm{HMF}_i}}{C_{\mathrm{HMF}_i}}\right) \times 100 \tag{1}$$

where C_{HMF} represents the number of moles of HMF, and C_{HMF_i} and C_{HMF_f} correspond to the initial and final number of moles of HMF, respectively.

$$\mathrm{FDCA}_{\mathrm{Selectivity}} = \left(\frac{C_{\mathrm{FDCA}}}{C_{\mathrm{HMFCA}} + C_{\mathrm{FFCA}} + C_{\mathrm{DFF}} + C_{\mathrm{FDCA}}}\right) \times 100 \tag{2}$$

where C_{FDCA} is the number of moles of FDCA, and C_{HMFCA}, C_{FFCA}, and C_{DFF} are the intermediate or final products involved in the reaction.

$$\mathrm{C.B.} = \left(\frac{C_{\mathrm{HMF}_f} + C_{\mathrm{HMFCA}} + C_{\mathrm{DFF}} + C_{\mathrm{FFCA}} + C_{\mathrm{FDCA}}}{C_{\mathrm{HMF}_i}}\right) \times 100 \tag{3}$$

where C_{HMF}, C_{FDCA}, C_{HMFCA}, C_{FFCA}, and C_{DFF} are the number of moles of HMF and its oxidation products, used to evaluate the overall carbon conservation.

Error bars represent the standard deviation of replicate measurements with Au/ZrO_2, indicating an approximate 5% uncertainty in product conversion, carbon balance and product selectivity.

3 Results and discussion

3.1 Characterization of Au@MnO_2

The optical response of the synthesized AuNPs and their core-shell derivatives (Au@MnO_2) was examined via UV-Vis spectroscopy to monitor changes in LSPR. Figure S1 shows the time-dependent UV-Vis spectral evolution during the reduction process of AuNPs. As shown in Fig. 2, the pristine AuNPs exhibit a characteristic LSPR peak around 580 nm. Upon MnO_2 shell deposition —achieved through the controlled addition of $KMnO_4$— a systematic red-shift in the LSPR band was observed, reaching 600 nm for the thickest shell (10 nm). This shift reflects the increasing local refractive index around the Au core, confirming the successful formation of the core-shell structure.

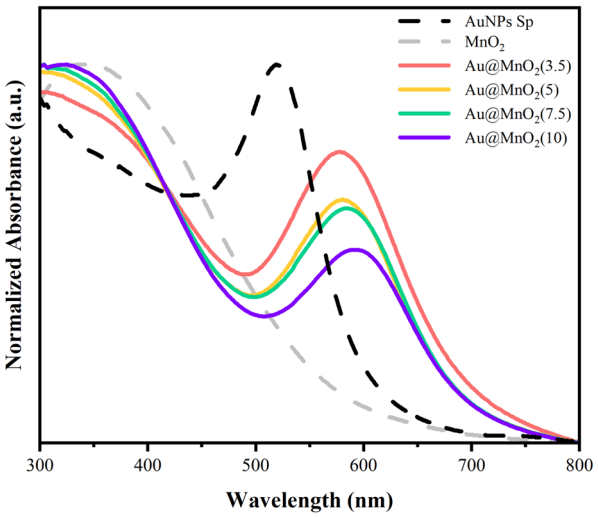

Fig. 2 UV-VIS spectra of Au@MnO_2 core-shell nanoparticles for different shell thicknesses (3.5 nm, 5 nm, 7.5 nm, 10 nm) and comparison with AuNPs and MnO_2 spectra. The spectrum is normalized for the extinction at the top of the LSPR band

The degree of the LSPR shift correlated with the nominal MnO_2 shell thickness, following the sequence: Au@MnO_2 (10 nm) >7.5 nm >5 nm >3.5 nm. Additionally, a broad absorption feature near 320 nm appeared in the Au@MnO_2 spectra, attributable to the electronic transitions of the MnO_2 shell [24]. These results demonstrate that UV-Vis spectroscopy provides a rapid and effective means to confirm shell formation and assess relative shell thickness in Au@MnO_2 nanostructures, with spectral changes directly linked to modifications in the optical environment and composition.

The morphology and shell formation of the AuNPs and Au@MnO_2 core-shell nanostructures were investigated using SEM, as shown in Figs. S5 and S6. The images clearly reveal the formation of a manganese oxide shell surrounding the Au cores for all targeted thicknesses–3.5 nm, 5 nm, 7.5 nm, and 10 nm (S6.a-S6.d, respectively). The progressive reduction in MnO_2 shell thickness across samples is readily distinguishable, confirming the effectiveness of the controlled synthesis approach. In all cases, the gold core is centrally located and uniformly coated with a spiky MnO_2 shell–a morphology typical of this oxide and indicative of its nanostructured growth behavior. The shell coverage appears consistent, suggesting a high degree of reproducibility in the deposition process. After loading onto ZrO_2, SEM images were taken (Fig. S9), confirming good dispersion of the catalyst on the support. Long-term stability was also assessed: SEM images taken one year later (Fig. S7) demonstrate that the core–shell structure remained intact in an aqueous environment. To verify the composition of the nanoparticles, energy dispersive X-ray analysis (EDX) was performed (Fig. S8). The spectrum indicates high purity, with only Au and MnO_2 detected; the presence of aluminium (Al) arises from the support and can therefore be disregarded.

TEM further substantiates the core-shell architecture, as shown in Fig. 3. The high contrast between the darker Au core (15 nm) and the lighter MnO_2 shell allows for clear visualization of the nanostructure. Although precise thickness differentiation is limited by the resolution, particularly for highly uniform shells, a systematic increase in MnO_2 content from Fig. 3(a) to (d) aligns with the increasing $KMnO_4$ precursor concentration. Notably, samples with thinner MnO_2 layers exhibit closer particle proximity and slight agglomeration, likely due to insufficient shell coverage for effective colloidal stabilization. These results corroborate the UV-Vis and SEM data, reinforcing the successful fabrication of core-shell structures with tunable shell thicknesses.

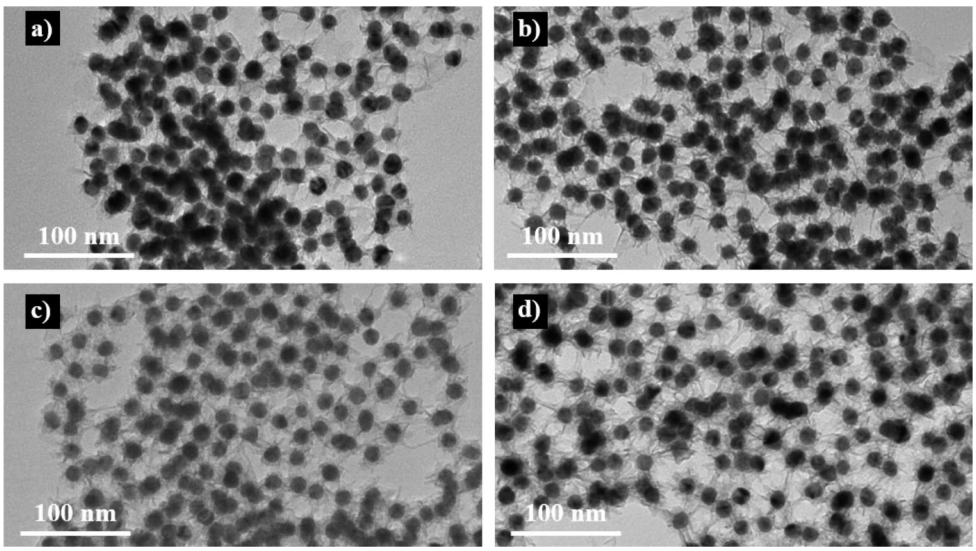

Fig. 3 TEM images of Au@MnO_2 with different thicknesses of MnO_2 layers: (a) 3.5 nm, (b) 5 nm, (c) 7.5 nm, and (d) 10 nm

The XRD analysis is presented in Fig. 4 further confirms material composition. Diffraction peaks at $2\theta \approx 38°$, 44°, and 65° are assigned to the (111), (200), and (220) planes of face-centered cubic Au, respectively [25, 26]. MnO_2 contributions are less pronounced, with broad and weak reflections consistent with amorphous or poorly crystalline phases, particularly evident in the broad feature around 65° assigned to the (220) plane of MnO_2 [25]. This low crystallinity is consistent with the thin, high-surface-area MnO_2 shell morphology observed in the TEM and SEM analyses.

Control experiments provided critical evidence for the core-shell configuration. As shown in Fig. S2, in the absence of $KMnO_4$, the LSPR peak of AuNPs remained unchanged, indicating no significant morphological alteration. UV-Vis spectra (Fig. S3) revealed minimal absorption in the 450–600 nm range when $KMnO_4$ remained unreacted, and only a weak increase in the 300–400 nm region, corresponding to MnO_2, suggesting limited $KMnO_4$ reduction in the absence of Au. SEM analysis of the control samples (Fig. S4) further corroborated these findings: in the absence of $KMnO_4$, significant AuNP agglomeration was observed (Fig. S4(a)), whereas MnO_2 -only samples exhibited the characteristic spiky morphology (Fig. S4(b)). In contrast, samples containing both components consistently displayed discrete, core-shell nanostructures (Fig. S6(a)-(d)), confirming the specific formation of Au@MnO_2 particles under the designed synthetic conditions.

3.2 Visible-light Assisted Oxidation of HMF over Au@MnO_2 nanoparticles

The catalytic activity of Au@MnO_2 supported on ZrO_2 was evaluated under both thermal (40°C) and photochemical conditions using LED illumination at 365 nm (UV) and 450 nm (visible light). Thermal reactions were conducted at 40 °C to match the temperature reached under LED irradiation, ensuring that observed differences in reactivity could be attributed to light-induced effects rather than thermal contributions. The results demonstrated a pronounced difference in reactivity between thermally driven and light-activated reactions, highlighting the photocatalytic nature of the Au@MnO_2 system.

To decouple the individual contributions of light and base, a series of blank experiments were performed under various illumination conditions in the absence of catalyst (Table 1). Under UV light (365 nm) and without NaOH, a high HMF conversion (62.5%) was observed; however, the poor selectivity and low carbon balance indicated extensive non-selective degradation. In contrast, both visible light (450 nm) and dark conditions resulted in negligible conversion, suggesting that light energy alone —especially in the visible range— is insufficient to drive HMF oxidation in the absence of catalytic material. The presence of NaOH improved overall system performance across all conditions, enhancing both conversion and selectivity. Notably, under UV light with base, the conversion decreased relative to the base-free case, but the selectivity towards desired oxidation

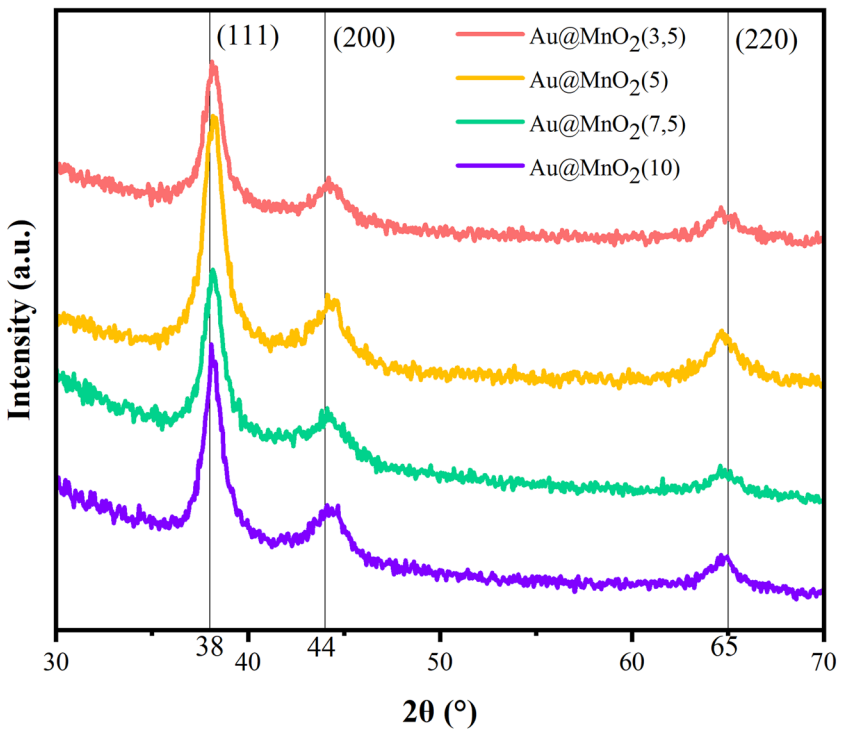

Fig. 4 X-ray powder diffraction of Au@MnO_2 core-shell nanoparticles for different shell thicknesses (3.5 nm, 5 nm, 7.5 nm, 10 nm)

Table 1 Blank tests under various illumination and reaction conditions, without catalyst, at ambient temperature and pressure

Light (nm)	NaOH	Conv. (%)	Sel. DFF (%)	Sel. HMFCA (%)	Sel. FDCA (%)	C.B. (%)
365	–	62.50	0.00	0.14	0.00	37.72
450	–	1.29	7.28	4.77	0.00	98.92
–	–	4.76	0.00	0.16	0.00	95.46
365	2:1	45.89	0.30	4.27	0.00	58.39
450	2:1	33.48	0.00	4.31	0.00	68.10
–	2:1	11.09	0.00	5.69	0.00	89.60

Table 2 Blank tests under different illumination and reaction conditions using 5 mg ZrO_2 alone and 5 mg unsupported MnO_2 nanomaterials: (1) nanowires (synthesized according to Ref. [27]) and (2) nanoflowers (synthesized according to Ref. [28])

Catalyst	Light (nm)	Conv. (%)	Sel. DFF (%)	Sel. HMFCA (%)	Sel. FFCA (%)	Sel. FDCA (%)	C.B. (%)
ZrO_2	–	14.8	0.00	11.56	0.89	0.00	87.04
ZrO_2	365	33.8	0.00	5.27	4.43	0.48	69.64
ZrO_2	450	33.51	0.00	35.70	2.03	0.40	79.27
MnO_2(1)	365	19.9	0.91	2.02	0.67	0.47	80.91
MnO_2(2)	365	30.46	0.35	0.07	0.32	0.32	69.87

All experiments were conducted at ambient temperature and pressure

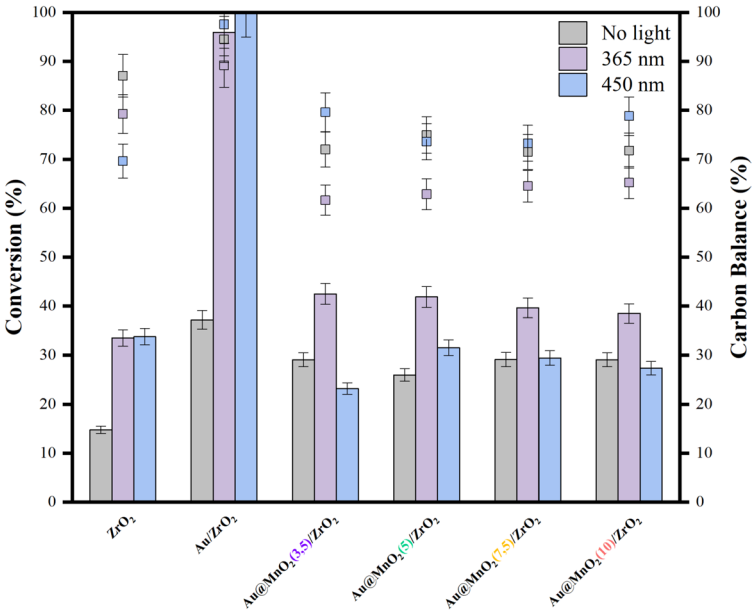

Fig. 5 Conversion of the HMF and carbon balance during the reaction performed at 40°C (in the dark) and under photochemical conditions at 365 nm and 450 nm, as a function of the catalyst used

products (e.g., HMFCA) increased significantly, suggesting a shift toward more controlled reaction steps. These findings underscore the critical role of the Au@MnO_2 catalyst in enabling selective, light-assisted HMF oxidation and demonstrate that neither light nor base alone is sufficient to achieve both high activity and selectivity. Table 2 summarizes the selectivity, conversion, and carbon balance obtained using ZrO_2 (as catalyst support) and MnO_2 nanomaterials. Although only partial HMF conversion was observed, negligible amounts of the desired products were formed, with HMFCA selectivity of 2% for MnO_2 nanowires and 0.3% for nanoflowers. Similarly, ZrO_2 exhibits low HMFCA selectivity after 4 h of reaction, reaching 35.7% under 450 nm irradiation, but decreasing to 5.27% at 365 nm and 11.56% in the dark.

Thermal catalytic tests conducted at 40°C without light irradiation resulted in modest HMF conversion, reaching approximately 30%, as shown in Fig. 5. The corresponding carbon balance remained low (72-75%), indicating significant degradation of either the substrate or intermediates during the thermal process. Among the observed products, 5-hydroxymethyl-2-furancarboxylic acid (HMFCA) was the only detectable oxidation product, with the Au@MnO_2 catalyst bearing a 10 nm MnO_2 shell achieving the highest productivity of 1.5 mol HMFCA per mol Au per hour (Fig. 6).

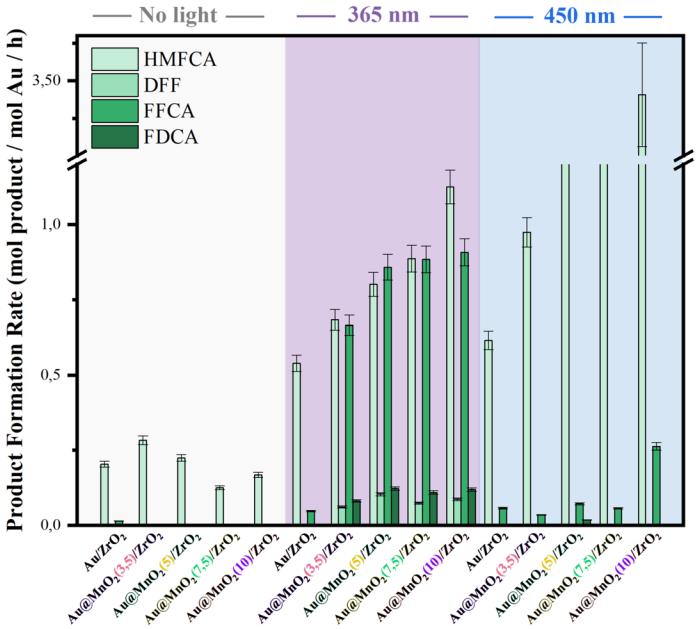

Fig. 6 Product formation rate during the reaction performed at 40°C (in the dark) and under photochemical conditions at 365 nm and 450 nm, as a function of the catalyst used

Under photochemical conditions, the reaction irradiated at 365 nm exhibited the highest overall activity. This enhanced performance is likely due to the overlap between the MnO_2 absorption edge and the UV light source, facilitating more effective photoexcitation of the catalyst. However, this higher activity was accompanied by a decrease in selectivity, as reflected by the lower carbon balance compared to thermal or visible-light (450 nm) conditions, suggesting increased formation of unquantified degradation products.

Figure 6 summarizes the product distributions obtained under thermal (dark) and photochemical conditions (365 nm and 450 nm) for all Au@MnO_2 catalysts with varying shell thicknesses. Productivities are reported as moles of product formed per mole of Au per hour. The data highlight clear differences in catalytic behavior depending on the excitation wavelength and shell thickness, with thicker MnO_2 shells generally correlating with higher activity.

Compared to thermal conditions, light-irradiated reactions demonstrated markedly enhanced catalytic activity, particularly under 365 nm illumination. This underscores the photocatalytic nature of the Au@MnO_2 system in driving HMF oxidation. A clear difference between the two excitation wavelengths was observed in both product distribution and selectivity. Under 365 nm irradiation, significant formation of HMFCA and FFCA were detected, along with smaller amounts of DFF and FDCA. In contrast, 450 nm irradiation predominantly yielded HMFCA, with only trace levels of FFCA, and FDCA was detected only in the catalyst bearing a 5 nm MnO_2 shell. These results demonstrate that the excitation wavelength critically influences the reaction pathway and product selectivity.

Notably, increased MnO_2 shell thickness correlated with enhanced catalytic activity across both wavelengths, consistent with improved light absorption and electron transfer capabilities. The product profiles also suggest a preferential reaction route via HMFCA, which is commonly favored in systems combining gold and manganese oxide catalysts [29]. DFF, a known intermediate, was only detected under 365 nm illumination and not at 450 nm,likely due to its high reactivity and tendency to either revert to HMF or proceed rapidly to FFCA and FDCA. This supports the hypothesis that different wavelengths selectively activate distinct oxidation pathways, potentially by modulating the involvement of photoexcited carriers or surface species.

While both HMFCA- and DFF-derived pathways appear plausible, the contribution of each to FDCA formation remains unclear. Additional mechanistic studies, such as time-resolved product analysis or isotopic labeling, are needed to resolve the specific intermediates and pathways involved. Nonetheless it is notable that AuNPs act as a photon antenna, enhancing light absorption and generating LSPR [30]. This LSPR excitation produces a high density of free electrons that interact with MnO_2 to generate reactive oxygen species (ROS) in aqueous medium, including hydrogen peroxide (H_2O_2), superoxide ($^{\bullet}O_2^-$), hydroxyl radicals ($^{\bullet}OH$), or singlet oxygen ($^1O_2$) which subsequently drive the oxidation of HMF to FDCA [31]. In the absence of MnO_2, AuNPs achieve high HMF conversion to HMFCA with limited progression along the oxydation pathway. In contrast, Au@MnO_2 core-shell structures generate comparable amounts of HMFCA and FFCA, indicating a more oxidative pathway and demonstrating that the core-shell architecture modulates the reaction mechanism

toward deeper oxidation. These preliminary results provide compelling evidence for the light-responsive nature of the Au@MnO_2 catalysts and their tunable selectivity. To further improve overall yields and maximize FDCA production, future work should consider extending reaction durations (e.g., 9-12 h [17]) or decreasing the substrate-to-catalyst ratio to increase the availability of accessible active sites. Kinetic studies over 10 h indicate sustained HMF conversion, suggesting that a 4 h reaction may be relatively short. However, 4 h was chosen as a standard to allow consistent comparisons across experiments. Figure S11 shows that catalysts with 7.5 nm and 10 nm MnO_2 shells maintain stable activity over the 10 h reaction, implying possible saturation of active sites which limits the reaction rate to approximately 0.2 mol product per mol Au per hour.

Table S3 presents a comparative overview of literature reports. To date, only three studies have explored the use of AuNPs supported on MnO_2 for HMF oxidation, and none have investigated the Au@MnO_2 core-shell architecture. Comparison of reaction rates emphasized the critical influence of the HMF-to-Au molar ratio. High conversion and selectivity can be achieved, but catalyst loading should be minimized relative to the substrate, especially in industrial FDCA production where cost reduction is critical. Operating under ambient temperature and pressure, with water as the solvent, further enhances process sustainability. While improvements in selectivity remain desirable, it is equally important to demonstrate that the productivity rate is significant, as illustrated in Fig. S11. Importantly, HMF does not convert into a single product but undergoes stepwise oxidation, ultimately forming FDCA.

4 Conclusion

In this study, we successfully synthesized Au@MnO_2 core-shell nanocatalysts with precisely controlled MnO_2 shell thicknesses ranging from 3.5 nm to 10 nm using a robust colloidal method. Structural and optical characterization confirmed the formation of well-defined core-shell architectures with preserved plasmonic properties. Preliminary photocatalytic tests demonstrated their effectiveness in selectively oxidizing HMF, with catalytic activity and product distribution strongly dependent on both MnO_2 shell thickness and irradiation wavelength. Notably, the core-shell design not only enhanced catalytic activity and selectivity but also improved stability under reaction conditions.

Despite these promising results, challenges remain in developing robust photocatalytic-plasmonic systems. As highlighted by Jacinto Sá et al. [32] hot carriers generated in AuNPs play a critical role in plasmonic reactivity, yet their ultrafast lifetimes and the coexistence of competing mechanisms (e.g., impact excitation and Auger heating) complicate mechanistic understanding and practical implementation. These findings emphasize the synergistic function of AuNPs in combination with the MnO_2 shell, while also illustrating the inherent limitations of mechanistic studies. Such investigations often require highly specific experimental conditions, make it challenging to isolate individual effects, and their interpretation within multi-step catalytic systems may remain incomplete. Another limitation concerns catalyst recovery and recycling, given the very small amount employed in each batch. While scale-up in larger reactors could enable recovery by centrifugation, an alternative would be to investigate continuous-flow operation, would allow catalyst stability and potential deactivation to be assessed more directly over extended reaction times.

These results highlight the potential of Au@MnO_2 nanostructures as tunable and efficient platforms for light-driven chemical transformations. Beyond biomass valorization, their modular architecture and photoresponsive properties make them promising candidates for broader applications in plasmonic catalysis, environmental remediation, and solar-to-chemical energy conversion. Future studies will focus on extending reaction times, optimizing catalyst loading, and elucidating mechanistic pathways to further enhance performance and deepen understanding of these hybrid nanocatalysts.

Supplementary Information The online version contains supplementary material available at https://doi.org/10.1007/s42247-025-01277-4.

Acknowledgements This work was supported by "Lorraine Université d'Excellence", as part of the France 2030 Program, under reference ANR-15-IDEX-04-LUE.

Author Contributions All authors contributed to the study conception and design. Material preparation, data collection and analysis were performed by Arthur Reymond, IbrahiM Abdelsalam and Filippo Pieretti. The first draft of the manuscript was written by Arthur Reymond and all authors, IbrahiM Abdelsalam, Filippo Pieretti, Nikolaos Dimitratos, Almudena Marti, Pedro H.C. Camargo, Robert Wojcieszak commented on previous versions of the manuscript. All authors read and approved the final manuscript.

Funding Open Access funding provided by University of Helsinki (including Helsinki University Central Hospital).

Declarations

Conflicts of Interest On behalf of all authors, the corresponding author states that there is no conflict of interest.

References

1. I. Khan, K. Saeed, I. Khan, Nanoparticles: properties, applications and toxicities. Arab. J. Chem. **12**(7), 908–931 (2019). https://doi.org/10.1016/j.arabjc.2017.05.011
2. R. Luque, P. Prinsen, Nanoparticle design and characterization for catalytic applications in sustainable. Chemistry (2019). https://doi.org/10.1039/9781788016292
3. J.H. Stenlid, T. Brinck, Extending the σ-hole concept to metals: an electrostatic interpretation of the effects of nanostructure in gold and platinum catalysis. J. Am. Chem. Soc. **139**(32), 11012–11015 (2017). https://doi.org/10.1021/jacs.7b05987
4. E. Peiris, S. Hanauer, T. Le, J. Wang, T. Salavati-Fard, P. Brasseur, E.V. Formo, B. Wang, P.H.C. Camargo, Controlling selectivity in plasmonic catalysis: switching reaction pathway from hydrogenation to homocoupling under visible-light irradiation. Angew. Chem. Int. Ed. **62**(4), 1521–3773 (2023). https://doi.org/10.1002/anie.202216398
5. P.H.C. Camargo, E. Cortés, Plasmonic catalysis: from fundamentals to applications. WILEY-VCH GmbH, Germany (2021). https://doi.org/10.1002/9783527826971
6. K.Y. Kim, Plasmonics - principles and applications. IntechOpen, Rijeka (2012). https://doi.org/10.5772/2633
7. K.L. Kelly, E. Coronado, L.L. Zhao, G.C. Schatz, The optical properties of metal nanoparticles: the influence of size, shape, and dielectric environment. J. Phys. Chem. B **107**(3), 668–677 (2003). https://doi.org/10.1021/jp026731y
8. O. Pluchery, M. Carrière, Nanoparticules d'or. Techniques de l'Ingénieur. (2011)
9. A. Lancien, R. Wojcieszak, E. Cuvelier, M. Duban, P. Dhulster, S. Paul, F. Dumeignil, R. Froidevaux, E. Heuson, Hybrid conversion of 5-hydroxymethylfurfural to 5-aminomethyl-2-furancarboxylic acid: toward new bio-sourced polymers. ChemCatChem **13**(1), 247–259 (2021). https://doi.org/10.1002/cctc.202001446
10. R. Singh, R. Bhateria, Core–shell nanostructures: a simplest two-component system with enhanced properties and multiple applications. Environ. Geochem. Health **43**(7), 2459–2482 (2021). https://doi.org/10.1007/s10653-020-00766-1
11. E. Hayashi, Y. Yamaguchi, K. Kamata, N. Tsunoda, Y. Kumagai, F. Oba, M. Hara, Effect of mno(2) crystal structure on aerobic oxidation of 5-hydroxymethylfurfural to 2,5-furandicarboxylic acid. J. Am. Chem. Soc. **141**(2), 890–900 (2019). https://doi.org/10.1021/jacs.8b09917
12. A.G.M. Silva, T.S. Rodrigues, E.G. Candido, I.C. Freitas, A.H.M. Silva, H.V. Fajardo, R. Balzer, J.F. Gomes, J.M. Assaf, D.C. Oliveira, N. Oger, S. Paul, R. Wojcieszak, P.H.C. Camargo, Optimization of 5-hydroxymethylfurfural oxidation via photo-enzymatic cascade process. Green Chem. **26**, 8211–8219 (2024). https://doi.org/10.1039/D4GC00673A
13. D. Zhao, T. Su, Y. Wang, R.S. Varma, C. Len, Recent advances in catalytic oxidation of 5-hydroxymethylfurfural. Molecular Catalysis. **495**, 111133 (2020). https://doi.org/10.1016/j.mcat.2020.111133
14. T. Oyegoke, F. Dumeignil, B. El-Yakubu Jibril, C. Michel, R. Wojcieszak, Exploring catalytic oxidation pathways of furfural and 5-hydroxymethyl furfural into carboxylic acids using Au, Pt, and Pd catalysts: a comprehensive review. Catal. Sci. Technol. **14**, 6761–6774 (2024). https://doi.org/10.1039/D4CY00821A
15. Y. Guo, Y. Zhao, S. Gao, B. Lv, Z. Wu, Noble metal-based catalysts for selective oxidation of HMF to FDCA: progress in reaction mechanism and active sites. Chemistry **7**(1), 17 (2025). https://doi.org/10.3390/chemistry7010017
16. M. Niakan, P. Ghamari Kargar, B. Maleki, R.S. Zabibah, M. Daryapeima, S. Sedigh Ashrafi, S. Zhou, Ternary $\mathrm{agfe_2\ o_4/sba\text{-}16/so_3\ h}$ heterojunction photocatalyst for the sustainable production of 5-hydroxymethylfurfural under mild conditions. Langmuir **41**(21), 13220–13232 (2025). https://doi.org/10.1021/acs.langmuir.5c00894
17. P. Khajegi, M. Rashidi Huyeh, B. Palpant, M. Maleki, Thermo-optical properties of gold nanoparticles: shape and size effects. Plasmonics (2024). https://doi.org/10.1007/s11468-024-02630-9
18. T. Oyegoke, A. Sadier, S. Navarro-Jaén, A. Ventimiglia, N. Dimitratos, F. Dumeignil, B. El-Yakubu Jibril, R. Wojcieszak, C. Michel, Enhancing 5-hydroxymethylfurfural oxidation to 2,5-furan-dicarboxylic acid with au-supported catalysts: optimizing reaction parameters and unraveling degradation mechanism through dft calculations. Catal. Today **445**, 115086 (2025). https://doi.org/10.1016/j.cattod.2024.115086
19. T. Yamaguchi, Application of $\mathrm{zro_2}$ as a catalyst and a catalyst support. Catal. Today **20**(2), 199–217 (1994). https://doi.org/10.1016/0920-5861(94)80003-0
20. O. Ishchenko, V. Rogé, G. Lamblin, D. Lenoble, I. Fechete, $\mathrm{tio_2}$, zno, and $\mathrm{sno_2}$-based metal oxides for photocatalytic applications: principles and development. C. R. Chim. **24**(1), 103–124 (2021). https://doi.org/10.5802/crchim.64
21. J. Quiroz, E.C.M. Barbosa, T.P. Araujo, J.L. Fiorio, Y.-C. Wang, Y.-C. Zou, T. Mou, T.V. Alves, D.C. Oliveira, B. Wang, S.J. Haigh, L.M. Rossi, P.H.C. Camargo, Controlling reaction selectivity over hybrid plasmonic nanocatalysts. Nano Lett. **18**(11), 7289–7297 (2018). https://doi.org/10.1021/acs.nanolett.8b03499
22. A.G. Silva, T.S. Rodrigues, V.G. Correia, T.V. Alves, R.S. Alves, R.A. Ando, F.R. Ornellas, J. Wang, L.H. Andrade, P.H. Camargo, Plasmonic nanorattles as next-generation catalysts for surface plasmon resonance-mediated oxidations promoted by activated oxygen. Angewandte Chemie (International ed. in English). **55**(25), 7111–7115 (2016). https://doi.org/10.1002/anie.201601740
23. G.P. Oliveira, T.B.V. Neves, L.P.F. Peixoto, S.M. Landi, B.S. Archanjo, G.F.S. Andrade, Synthesis and characterization of $\mathrm{au@mno_2}$ nanoparticles as plasmon enhanced spectroscopy substrates. Journal of the Brazilian Chemical Society (2023). https://doi.org/10.21577/0103-5053.20220146
24. M. Gao, Y. Song, Y. Liu, W. Jiang, J. Peng, L. Shi, R. Jia, Y. Muhammad, L. Huang, Controlled fabrication of $\mathrm{au@mno_2}$ core/shell assembled nanosheets by localized surface plasmon resonance. Appl. Surf. Sci. **537**, 147912 (2021). https://doi.org/10.1016/j.apsusc.2020.147912
25. X. Zhou, G. Zhao, M. Chen, W. Gao, X. Zhou, X. Xie, L. Yang, G. Du, Facile and green approach to prepare nanostructured $\mathrm{au@mno_2}$ and its applications for catalysis and fluorescence sensing of glutathione in human blood. ACS Sustain. Chem. Eng. **6**(3), 3948–3956 (2018). https://doi.org/10.1021/acssuschemeng.7b04313
26. X. Hu, C. Quan, T. Ren, L. Zhao, Y. Shen, Y. Zhu, J. Wang, $\mathrm{mno_2}$ nanoparticles decorated with Ag/Au nanotags for label-based SERS determination of cellular glutathione. Mikrochim. Acta **190**(8), 341 (2023). https://doi.org/10.1007/s00604-023-05870-4
27. C.P. Ferraz, A.G.M. Da Silva, T.S. Rodrigues, P.H.C. Camargo, S. Paul, R. Wojcieszak, Furfural oxidation on gold supported on $\mathrm{mno_2}$: influence of the support structure on the catalytic

performances. Appl. Sci. **8**(8), 1246 (2018). https://doi.org/10.3390/app8081246
28. A.G.M. Silva, T.S. Rodrigues, E.G. Candido, I.C. Freitas, A.H.M. Silva, H.V. Fajardo, R. Balzer, J.F. Gomes, J.M. Assaf, D.C. Oliveira, N. Oger, S. Paul, R. Wojcieszak, P.H.C. Camargo, Combining active phase and support optimization in mno_2-au nanoflowers: enabling high activities towards green oxidations. J. Colloid Interface Sci. **530**, 282–291 (2018). https://doi.org/10.1016/j.jcis.2018.06.089
29. S. Chen, R. Wojcieszak, F. Dumeignil, E. Marceau, S. Royer, How catalysts and experimental conditions determine the selective hydroconversion of furfural and 5-hydroxymethylfurfural. Chem. Rev. **118**(22), 11023–11117 (2018). https://doi.org/10.1021/acs.chemrev.8b00134
30. C.L. Brosseau, E. Cortés, Charting a new course with plasmon-mediated chemistry. Commun. Chem. **7**(1), 294 (2024). https://doi.org/10.1038/s42004-024-01340-x
31. P. Ghamari Kargar, B. Maleki, M. Ghani, $ag/go/fe_3o_4/\gamma - fe_2o_3$ nanocomposite for green-light-driven photocatalytic oxidation of 5-hydroxymethylfurfural to 5-hydroxymethyl-2-furancarboxylic acid. ACS Appl. Nano Mater. **7**(8), 8765–8782 (2024). https://doi.org/10.1021/acsanm.4c00223
32. A. Wach, R. Bericat-Vadell, C. Bacellar, C. Cirelli, P.J.M. Johnson, R.G. Castillo, V.R. Silveira, P. Broqvist, J. Kullgren, A. Maximenko, T. Sobol, E. Partyka-Jankowska, P. Nordlander, N.J. Halas, J. Szlachetko, J. Sá, The dynamics of plasmon-induced hot carrier creation in colloidal gold. Nat. Commun. **16**(1), 2274 (2025). https://doi.org/10.1038/s41467-025-57657-1